Effects of Core Distances, Solvent, Ligand, and Level of Theory on the TDDFT Optical Absorption Spectrum of the Thiolate-Protected Au_{25} Nanoparticle

Christine M. Aikens

Department of Chemistry, Kansas State University, Manhattan, Kansas 66506

Received: June 2, 2009; Revised Manuscript Received: August 3, 2009

Density functional theory calculations are employed to calculate geometries (R = H, CH_3, CH_2CH_3, CH_2CH_2Ph) and excitation energies (R = H, CH_3, CH_2CH_3) for the $Au_{25}(SR)_{18}^-$ nanoparticle. The splitting between the first two peaks in the optical absorption spectrum is known to arise as a result of ligand-field splitting of superatom D orbitals, and the value of this splitting is found to be a very sensitive probe of gold−gold distances in the $Au_{25}(SH)_{18}^-$ nanoparticle core. LDA functionals such as Xα with a triple-ζ basis set are found to predict core geometries in good agreement with experiment, which suggests that this level of theory may be useful in future structural predictions. Asymptotically correct potentials SAOP and LB94 with triple-ζ basis sets yield excitation energies within 0.15−0.20 eV of experimental values; LB94 with a frozen-core basis set is found to be an inexpensive alternative to the preferred SAOP potential. The size of the ligand plays a minor role on the optical absorption spectrum and solvent effects on geometries and excitation energies are negligible, which demonstrates that the core geometric and electronic structure is primarily responsible for the discrete optical absorption exhibited by this nanoparticle.

Introduction

Monolayer-protected gold nanoparticles are of considerable interest because of their unique biological, catalytic, optical, and electronic applications.[1−4] One of the striking characteristics of noble metal nanoparticles is strong surface plasmon absorption that leads to a sharp peak in the visible region of the optical spectrum. However, thiolated gold nanoclusters with diameters less than approximately 2 nm display a series of discrete absorption features that scale with size.[5] In this regime, several core cluster sizes exhibit remarkable stability, including $Au_{20}(SR)_{16}$, $Au_{25}(SR)_{18}$, $Au_{38}(SR)_{24}$, $Au_{102}(SR)_{44}$, $Au_{140-156}(SR)_{50-60}$, and so forth, where R may be one of several organic groups.[5−10] The remarkable observation of discrete optical peaks for these nanoclusters as opposed to the single plasmon resonance of larger nanoparticles and the possible structure−property relationships that govern this variation are not fully understood.

Recent total structure determination of $Au_{102}(p\text{-SPhCOOH})_{44}$[7] and $[Au_{25}(SCH_2CH_2Ph)_{18}^-]$[11,12] (Ph = phenyl) identified decahedral and icosahedral cores surrounded by linear −S−Au−S− "staple" **1** and V-shaped −S−Au−S−Au−S− **2** motifs, which provide clues to the exceptional stability of these clusters. Using patterns observed in Au_{102}, an independent density functional theory (DFT) investigation correctly predicted the structure of $Au_{25}(SR)_{18}^-$.[13] The structure of the $Au_{25}(SR)_{18}^-$ nanoparticle consists of an approximately icosahedral Au_{13} core surrounded by six −S−Au−S−Au−S− motifs in an almost D_{2h} arrangement (Figure 1). This nanoparticle exists in several charge states, and the neutral $Au_{25}(SR)_{18}$ structure has been shown by X-ray crystallography to be similar to its anionic counterpart.[14] A similar structure is also predicted to be the lowest energy for $Au_{25}(SR)_{18}^+$,[13] whereas prior DFT studies had suggested that the cation structure consists of a planar Au_7 core surrounded by one $Au_{12}(SR)_{12}$ and two $Au_3(SR)_3$ cyclic oligomers.[15]

Motifs such as **1** and **2** are also expected on larger gold nanoparticles[16] and surfaces.[17,18] Future experimental and theoretical investigations will likely resolve whether or not these motifs are responsible for the discrete absorption features displayed by gold nanoclusters. In order to do this, the structures of these systems must be known. Close agreement between experimentally observed and theoretically predicted properties can be used to assign structures to nanoparticles whose crystal structures have not been solved. As an example, several structures have been debated for $Au_{38}(SR)_{24}$ including a bi-icosahedral Au_{23} core surrounded by three **1** and six **2** motifs,[19] a face-centered cubic (fcc), bi-icosahedral, or bicapped Au_{25} core with nine **1** and two **2** motifs,[20] a disordered core surrounded by six **1** and four **2** motifs[21] or three **1** and four **2** motifs,[22] a Au_{14} core surrounded by six $(AuSR)_4$ cyclic units,[23] a disordered structure,[24,25] and a truncated octahedral fcc Au_{38} core surrounded by 24 SR units.[26] Zeng et al. predicted optical absorption spectra for their proposed structures, but the number and the locations of the peaks differ from the experimental data.[19] Häkkinen et al. also predict a series of discrete absorption features for their cluster, but the overall spectrum differs from experiment.[23] Accurate calculation of the optical absorption spectrum for each of these systems could be used to aid in the resolution of the geometrical structure.

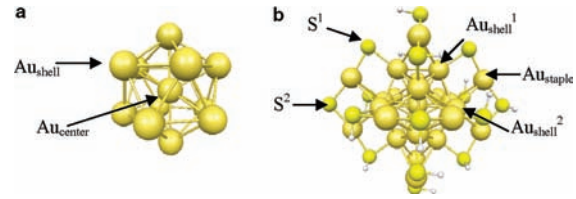

Figure 1. Structure of $Au_{25}(SR)_{18}^-$. (a) Approximately icosahedral core consisting of a central gold atom surrounded by a shell of 12 gold atoms. (b) Nearly D_{2h} arrangement of six V-shaped −S−Au−S−Au−S− motifs surrounding the 13-atom gold core.

In previous work, time-dependent density functional theory (TDDFT) has been effectively employed to assign transitions observed in the experimental UV−vis spectrum of the

10.1021/jp9051853 CCC: $40.75
Published on Web 09/11/2009

$Au_{25}(SCH_2CH_2Ph)_{18}^-$ nanoparticle using a model $Au_{25}(SH)_{18}^-$ system.[12] This prior investigation yielded a semiquantitative correlation between the experimental and theoretical optical absorption spectra. Three well-defined bands were observed experimentally at 1.8, 2.75, and 3.1 eV after redissolving $Au_{25}(SCH_2CH_2Ph)_{18}^-$ crystals in toluene. Gas-phase TDDFT calculations using the SAOP/TZP level of theory on a $Au_{25}(SH)_{18}^-$ structure optimized at the BP86/TZP.4f level of theory predicted bands at 1.52, 2.63, and 2.91 eV. However, the splitting between the first two bands in the spectrum is predicted to be 1.11 eV at the SAOP/TZP//BP86/TZP.4f level of theory, whereas the experimentally determined splitting is 0.95 eV.[12] The electronic shell model in which valence electrons of metal atoms combine to form delocalized S, P, D, ... "superatom" orbitals has been commonly used to explain the stability of alkali- and noble-metal clusters[27] and has recently been employed to elucidate the stability of various bare and monolayer-protected gold nanoparticles in the 1−2 nm size regime.[28,29] The splitting observed in the optical absorption spectrum of the $Au_{25}(SR)_{18}^-$ nanoparticle can be understood to arise from transitions out of an approximately triply degenerate P-type HOMO into a doubly degenerate D-type LUMO and a triply degenerate D-type LUMO+1; the five superatom D orbitals are split by the approximately octahedral field of the V-shaped ligand motifs.[13,30] Thus, the splitting reflects the structure of the nanoparticle and it is critical to compute this value precisely.

Although the previously calculated peak positions and peak splitting are within the accuracy typically expected for TDDFT, several potentially controllable sources of error remain, including the choice of model ligand (SH, SCH_3, SCH_2CH_3, SCH_2CH_2Ph, etc.), solvation condition of the compound (gas-phase vs toluene or other solvent), and the choice of method/basis set in the geometry optimization and excitation calculations. Although these differences are small enough to facilitate assignment of the transitions, improved agreement between experiment and theory would aid in future prediction of the structures of other small nanoparticles. Toward this end, this paper reports a study of the relative importance of the physical model (inclusion of solvent, choice of model ligands, etc.) and theoretical methods that can be employed to calculate gold nanoparticle geometrical structures and optical absorption spectra.

Computational Details

Several local density approximation (LDA), generalized gradient approximation (GGA), hybrid, and meta-GGA exchange-correlation functionals are utilized in this work. LDAs employed include Xα, Xonly, and the Vosko-Wilk-Nusair (VWN)[31] functionals. GGAs utilized include Xu and Goddard exchange[32] with Lee−Yang−Parr correlation[33] (XLYP), OPTX exchange[34] with Perdew−Burke−Ernzerhof correlation[35] (OPBE), the KT1 and KT2 functionals of Keal and Tozer,[36] and several other GGA functionals described in the Supporting Information. Tao−Perdew−Staroverov−Scuseria (TPSS),[37] PBE0,[38] and other meta-GGA and hybrid functionals as well as ab initio methods have also been employed as described in the Supporting Information; these calculations utilize the GAMESS program[39] and employ the Stevens−Basch−Krauss−Jasien−Cundari (SBKJC) effective core potential[40−42] and improved model core potential (IMCP)[43,44] scalar relativistic basis sets for gold. All GGA and LDA calculations are performed using the Amsterdam Density Functional (ADF) 2007.01 program.[45] Slater type basis sets employed in the ADF calculations include a double-ζ basis set with a [$1s^2$-$4f^{14}$] frozen core for Au, a [$1s^2$-$2p^6$] frozen core for S, and a [$1s^2$] frozen core for C (denoted DZ.4f); an analogous polarized triple-ζ frozen core (TZP.4f) basis set; a TZP basis set with a [$1s^2$-$4d^{10}$] frozen core for Au (TZP.4d); full-core double-ζ (DZ), triple-ζ plus polarization (TZP), and triple-ζ with two polarization functions (TZ2P) basis sets; and a quadruple-ζ basis set with four polarization functions (QZ4P). Scalar relativistic effects were included by utilizing the zeroth-order regular approximation (ZORA).[46] The SCF convergence was tightened to 10^{-8}. A gradient convergence criterion of 10^{-3} and an energy convergence criterion of 10^{-4} were used in order to obtain well-converged geometries for the Au_{13}^{+5}, $Au_{25}(SH)_{18}^-$, and $Au_{25}(SCH_3)_{18}^-$ systems; the default convergence criteria were utilized for $Au_{25}(SCH_2CH_3)_{18}^-$ and $Au_{25}(SCH_2CH_2Ph)_{18}^-$.

Using the ADF program, TDDFT was used to determine energetics and compositions of excited states for $Au_{25}(SR)_{18}^-$. Model potentials used in these calculations include the asymptotically correct exchange functional of Van Leeuwen and Baerends (LB94),[47] the gradient-regulated asymptotic correction (GRACLB),[48] and the statistical average of orbital potentials (SAOP).[49,50] Excitations to the lowest 200 states were evaluated for the optical absorption spectra. The absorption spectra were fit with a Lorentzian function with a width at half-maximum of 0.2 eV. The conductor-like screening model (COSMO)[51] is employed for treating implicit solvation effects on the excitation spectra where noted below. The COSMO implementation in ADF[52] accounts for the effects of solvent polarization on the Kohn−Sham orbitals and orbital energies.

The notation B//A is utilized in this paper, where A represents the method/basis set used in the geometry optimization and B corresponds to the method/basis set employed in the TDDFT excitation calculation if this differs from A. For example, SAOP/TZP//Xα/TZP.4f represents a SAOP excitation calculation using a full core TZP basis set at the Xα/TZP.4f geometry. LB94//Xα/DZ.4f corresponds to a LB94 excitation calculation using the DZ.4f basis set at the Xα/DZ.4f geometry.

Results and Discussion

Au_{13}^{+5} Core Geometry. The $Au_{25}(SCH_2CH_2Ph)_{18}^-$ nanoparticle may be viewed as an approximately icosahedral Au_{13}^{+5} core surrounded by six $[Au_2(SR)_3]^-$ motifs (Figure 1). This idealized core is excellent from both geometric and electronic considerations as it possesses eight electrons, which is a common electron-shell filling in superatom clusters. From the crystal structure coordinates of $Au_{25}(SCH_2CH_2Ph)_{18}^-$, the distances from the central Au atom to the shell of Au atoms surrounding range from 2.774−2.793 Å with an average of 2.782 Å.[12] It should be noted that the optical absorption spectra are taken in solution whereas the X-ray structure determination was performed in the solid phase, so it is possible that the gold−gold distances in solution may vary slightly from the crystal structure coordinates. At the BP86/TZP.4f level of theory (from ref 12), the average center-shell distance in $Au_{25}(SH)_{18}^-$ is 2.853 Å, which is 0.071 Å longer than the distances derived from the crystal structure. The Au_{13}^{+5} core model reproduces the theoretical $Au_{25}(SH)_{18}^-$ distances well; the average center-shell distance in this model compound is 2.851 Å, so the Au_{13}^{+5} core model yields core distances that vary by only 0.002 Å from the $Au_{25}(SH)_{18}^-$ distances. However, the BP86/TZP.4f level of theory predicts center-shell distances for Au_{13}^{+5} that are approximately 0.07 Å too long relative to the experimental coordinates.

As described in more detail in Supporting Information, increasing the basis set size decreases the predicted center-shell distance. Several LDA, GGA, meta-GGA, and hybrid function-

TABLE 1: Average Au−Au Distance from Central Atom to Icosahedral Shell

functional	Au_{13}^{+5}	$Au_{25}(SH)_{18}^{-}$
XLYP/TZP.4f	2.830	2.845
Xonly/TZP.4f	2.799	2.816
OPBE/TZP.4f	2.798	*b*
KT1/TZP.4f	2.792	2.804
KT2/TZP.4f	2.769	2.781
Xα/TZP.4f	2.769	2.786
VWN/TZP.4f	2.754	2.774
PBE0/IMCP	2.821	*b*
TPSS/IMCP	2.789	*b*
experiment[a]		2.782

[a] $Au_{25}(SCH_2CH_2Ph)_{18}^{-}$ crystal structure geometry from ref 12. [b] Unphysical structures encountered in optimization. See text.

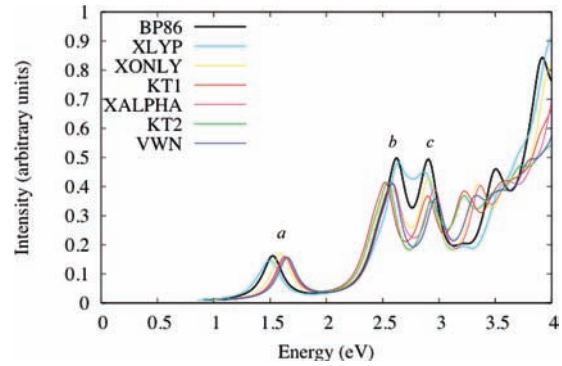

Figure 2. SAOP/TZP optical absorption spectrum for $Au_{25}(SH)_{18}^{-}$. The geometry of the nanoparticle is computed with the listed functionals.

TABLE 2: Calculated SAOP/TZP Optical Absorption Peaks (eV) for $Au_{25}(SH)_{18}^{-}$

geometry	peak a	peak b	peak c	a-b splitting
BP86[a]	1.52	2.63	2.91	1.11
XLYP	1.52	2.64	2.90	1.12
KT1	1.64	2.53	2.91	0.89
KT2	1.65	2.55	2.95	0.90
Xonly	1.60	2.56	2.91	0.96
Xα	1.63	2.59	2.97	0.96
VWN	1.65	2.59	2.98	0.94
experiment[b]	1.8	2.75	3.1	0.95

[a] Reference 12. [b] $Au_{25}(SCH_2CH_2Ph)_{18}$- from ref 12.

als have been examined in addition to Hartree−Fock and MP2 ab initio methods (see Supporting Information). Most GGA and hybrid functionals examined in this work overestimate the average Au−Au core distances; however, prior research on thiolated gold nanoparticle structural prediction has primarily employed the PBE[13,19,23] and B3LYP[15,53] functionals. Earlier work on gold has also shown that GGAs tend to overestimate Au−Au bond distances, which is related to the common observation that lattice constants predicted by GGAs tend to be too long whereas those determined by LDAs are often slightly underestimated.[54,55] In this work, functionals that predict center-core distances within 0.05 Å of the experimental value include three LDA functionals (Xα, Xonly, and VWN), four GGA functionals (OPBE, XLYP, KT1, and KT2), the hybrid PBE0 functional, and the meta-GGA TPSS functional (Table 1). These functionals have been subsequently utilized in geometry optimizations of the $Au_{25}(SH)_{18}^{-}$ nanoparticle.

Influence of Core Distances on $Au_{25}(SH)_{18}^{-}$ Optical Absorption Spectra. Geometry optimizations of the $Au_{25}(SH)_{18}^{-}$ nanoparticle were performed using nine functionals (Xα, Xonly, VWN, KT1, KT2, XLYP, OPBE, PBE0, and TPSS) that predict Au_{13}^{+5} core distances within 0.05 Å of the value derived from the crystal structure. Optimizations using OPBE lead to an octahedral core with poor Au−S bond lengths and angles, so this functional is not further considered here. Optimizations using PBE0/IMCP and TPSS/IMCP lead to structures in which the hydrogen atoms in the SH ligand point toward the core; this may be due to a deficiency in the hydrogen basis set used in conjunction with the IMCP set. The average center-shell distances for the other six functionals are summarized in Table 1. Further information on the optimizations and geometrical parameters are available in the Supporting Information. The functionals that predict the shortest gold−gold distances in the core also predict short distances between gold atoms in the ligand motifs and gold atoms in the core (Table S3 in Supporting Information).

TDDFT calculations using the SAOP/TZP level of theory have been performed at the BP86, XLYP, KT1, KT2, Xonly, Xα, and VWN geometries. The optical absorption spectra from these calculations are shown in Figure 2. In general, geometries with smaller center-shell distances lead to predictions for peak *a* that are slightly to the blue compared to those with larger center-shell distances. For peak *b*, smaller center-shell distances lead to predictions that are slightly to the red of those from larger distances. The overall effect is a decreased *a*-*b* splitting for geometries that closely match the gold coordinates from the experimental crystal structure. The first three peaks in the experimental spectrum lie at 1.8, 2.75, and 3.1 eV, and the splitting between the first two peaks is 0.95 eV.[12] At the Xα geometry, these peaks are predicted to lie at 1.63, 2.59, and 2.97 eV from excitation calculations at the SAOP/TZP level of theory (Table 2). Similarly, these peaks are computed to lie at 1.60, 2.56, and 2.91 eV for the Xonly geometry. This leads to an *a*-*b* splitting of 0.96 eV for Xα and Xonly. In comparison, the *a*-*b* splitting for SAOP/TZP calculations at the BP86 geometry is 1.11 eV.[12] From these results, it appears that *a*-*b* splittings in agreement with experiment may be obtained from structures with reasonable core geometries such as those obtained from Xα/TZP.4f and Xonly/TZP.4f geometry optimizations; thus, investigations of gold nanoparticles should employ functionals (such as the LDAs examined here) that can reliably predict gold−gold distances if these structures will be used for computation of response properties such as optical absorption spectra.

The stick and fitted optical absorption spectra for SAOP/TZP//Xα/TZP.4f are shown in Figure 3. The transitions responsible for these peaks are presented in Table 3. It should be noted that the first three excitation peaks (*a*, *b*, and *c*) calculated by TDDFT at 1.63, 2.59, and 2.95 eV are consistently underestimated by 0.15−0.20 eV relative to experiment. Density functional methods suffer from self-interaction error (SIE), which leads to excitation energies that are often somewhat underestimated. Before attributing the observed theory-experiment differences to SIE, it is necessary to investigate other physical differences in the two systems (solvent and ligand effects) as well as the dependence of the results on the level of theory employed in the excitation calculations.

Solvent Effects. Because the experimental UV−vis spectra are obtained in solvent and the theoretical optical absorption spectra to date have been computed in the gas phase, it is critical to analyze the effects of solvation on the absorption spectra. To measure the impact of solvation on the structure of the nanoparticle, an optimization of $Au_{25}(SH)_{18}^{-}$ in toluene using the COSMO implicit solvation model was performed with the

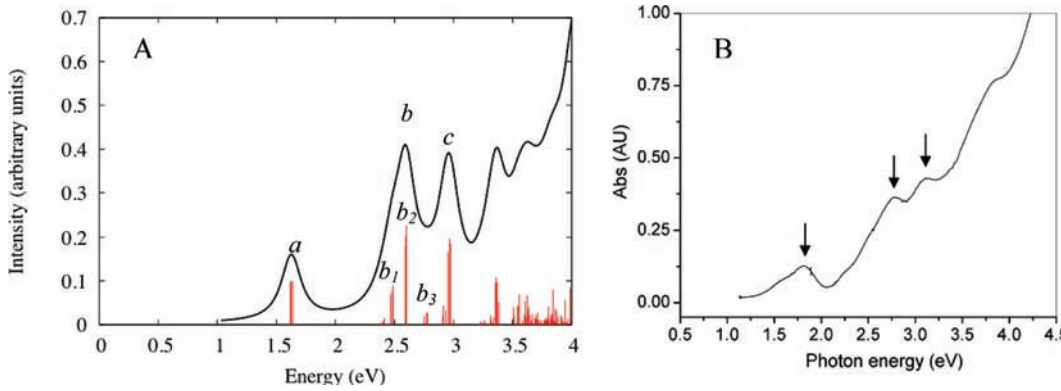

Figure 3. (A) SAOP/TZP optical absorption spectrum for $Au_{25}(SH)_{18}^-$ at the Xα/TZP.4f geometry. The stick spectrum determined from the TDDFT calculations is shown in red and the fitted spectrum is shown in black. (B) Experimental optical absorption spectrum from ref 12 (Copyright *J. Am. Chem. Soc.* **2008**, *130*, 5883−5885).

TABLE 3: Strong Optical Absorption Peaks in the Spectra of $Au_{25}(SH)_{18}^-$, the Transitions Responsible for These Peaks, and the Degeneracies (*g*) of the Orbitals Involved

peak	energy (eV)	transition from occupied orbital	*g*	transition to unoccupied orbital	*g*
a	1.63	HOMO	3	LUMO	2
b_1	2.48	HOMO-2	3	LUMO	2
b_2	2.59	HOMO	3	LUMO+1	3
b_3	2.77	HOMO	3	LUMO+2	1
c	2.97	HOMO-5	3	LUMO	2

Xα functional. This has negligible effects (∼0.001 Å and 0.03°) on nanoparticle bond lengths and angles (Table S3 in Supporting Information). In Figure 4, SAOP/TZP spectra at the Xα/TZP.4f geometry are shown for $Au_{25}(SH)_{18}^-$ in the gas phase and in toluene, methylene chloride, and acetonitrile. The height of the peak at 2.95 eV increases slightly as the solvent polarity increases, but in general the solvent does not greatly affect the absorption spectrum. These results agree with experimental findings that use of solvents other than toluene does not lead to appreciable peak shifting.[56] These results may be rationalized by considering that the highest occupied and lowest unoccupied Kohn−Sham orbitals are comprised primarily of atomic orbital contributions from the gold core,[12,30] which would not be greatly affected by solvent.

Ligand Effects. The second physical difference to be considered between the experimental and theoretical systems is the choice of ligand for $Au_{25}(SR)_{18}^-$. Since larger ligands often require less expensive computational methods for practical reasons, the relative accuracy trade-off is of interest in this work. In Table 4, the average center-shell distances for $Au_{25}(SR)_{18}^-$

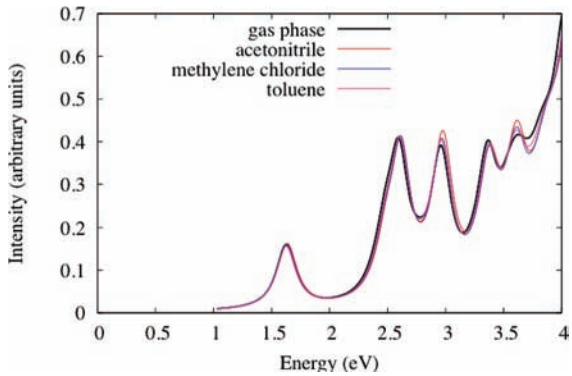

Figure 4. SAOP/TZP optical absorption spectrum in gas phase and in implicit solvent (COSMO) for $Au_{25}(SH)_{18}^-$ at the Xα/TZP.4f geometry.

TABLE 4: Average Au−Au Distance from Central Atom to Icosahedral Shell in $Au_{25}(SR)_{18}^-$

functional/basis	ligand	$Au_{center}-Au_{shell}$ (Å)
Xα/DZ.4f	R = H	2.784
	R = CH_3	2.787
	R = CH_2CH_3	2.788
	R = CH_2CH_2Ph	2.777
Xα/TZP.4f	R = H	2.786
	R = CH_3	2.791
	R = CH_2CH_3	2.799
experiment[a]	R = CH_2CH_2Ph	2.782

[a] $Au_{25}(SR)_{18}^-$ crystal structure geometry from ref 12.

with four model ligands (R = SH, SCH_3, SCH_2CH_3, SCH_2CH_2Ph) are shown with the Xα functional and the DZ.4f and TZP.4f basis sets. The average center-shell distance is relatively insensitive to the ligand used; with the DZ.4f level of theory, the H ligand overestimates the calculated CH_2CH_2Ph value by only 0.007 Å, while the CH_2CH_3 ligand overestimates this distance by 0.011 Å. Distances calculated with the TZP.4f basis set increase by 0.004−0.011 Å compared to the corresponding DZ.4f values. Although the geometry optimization of R = CH_2CH_2Ph is not currently feasible with the TZP.4f basis set, it is evident from Table 4 that the choice of model ligand does not greatly affect the predicted center-shell distances and that the Xα functional with both the DZ.4f and TZP.4f basis sets yields calculated values that are close to the experimental value.

In Table 5, orbital energy differences are calculated at several levels of theory for the four model ligands. The four orbital energy differences of interest are LUMO−HOMO (*a*), LUMO+1−HOMO (b_1), LUMO−HOMO-2 (b_2), and LUMO+3−HOMO (b_3), where the LUMO and HOMO designations include several nearly degenerate orbitals as determined from SAOP/TZP//Xα/TZP.4f calculations. This near-degeneracy has been discussed previously.[12,13,30] The orbital energies are calculated as the difference between the lowest energy orbital in the unoccupied set and the highest energy orbital of the occupied set; consequently, they underestimate the actual excitation energies by about 0.1−0.2 eV. However, they roughly correlate to peaks *a*, b_1, b_2, and b_3 in Figure 3.

For the SH ligand, SAOP/TZP slightly underestimates SAOP/TZ2P orbital energy differences by 0.00−0.02 eV, and orbital energy differences calculated using a frozen core TZP.4f basis set rather than a full core TZP basis set vary by 0.00−0.02 eV for LB94 and BP86 (Table 5). For SH, SCH_3, and SCH_2CH_3, GGA methods BP86 and PBE typically underestimate orbital

TABLE 5: Orbital energy differences for $Au_{25}(SR)_{18}^-$

R = SH	*a*	b_1	b_2	b_3
Xα/DZ.4f	1.300	1.724	1.807	2.368
BP86//Xα/DZ.4f	1.324	1.768	1.865	2.532
LB94//Xα/DZ.4f	1.407	1.889	1.989	2.575
SAOP/DZ//Xα/DZ.4f	1.425	1.936	1.983	2.696
Xα/TZP.4f	1.359	2.070	2.158	2.403
BP86//Xα/TZP.4f	1.392	2.130	2.227	2.625
BP86/TZP//Xα/TZP.4f	1.380	2.135	2.212	2.618
PBE/TZP//Xα/TZP.4f	1.379	2.129	2.212	2.566
LB94//Xα/TZP.4f	1.438	2.234	2.404	2.686
LB94/TZP//Xα/TZP.4f	1.429	2.241	2.413	2.686
SAOP/TZP//Xα/TZP.4f	1.477	2.291	2.389	2.734
SAOP/TZ2P//Xα/TZP.4f	1.480	2.293	2.389	2.756
R = SCH_3	*a*	*b*1	*b*2	*b*3
Xα/DZ.4f	1.221	1.657	1.718	2.334
BP86//Xα/DZ.4f	1.245	1.710	1.774	2.423
LB94//Xα/DZ.4f	1.307	1.797	1.936	2.538
SAOP/DZ//Xα/DZ.4f	1.345	1.866	1.931	2.717
Xα/TZP.4f	1.300	1.846	2.010	2.297
LB94/TZP//Xα/TZP.4f	1.365	1.999	2.267	2.585
SAOP/TZP//Xα/TZP.4f	1.400	2.079	2.254	2.649
R = SCH_2CH_3	*a*	b_1	b_2	b_3
Xα/DZ.4f	1.217	1.664	1.732	2.342
BP86//Xα/DZ.4f	1.240	1.717	1.791	2.428
LB94//Xα/DZ.4f	1.303	1.813	1.961	2.592
SAOP/DZ//Xα/DZ.4f	1.340	1.882	1.952	2.762
R = SCH_2CH_2Ph	*a*	b_1	b_2	b_3
Xα/DZ.4f	1.226	1.681	1.780	2.265
BP86//Xα/DZ.4f	1.249	1.735	1.840	2.317
LB94//Xα/DZ.4f	1.310	1.825	1.987	2.225[a]

[a] The LUMO+3 for R = SCH_2CH_2Ph arises from the phenyl groups. The next gold-basedorbital energy difference is 2.519 eV.

energy differences by 0.1−0.3 eV relative to SAOP, while Xα underestimates these differences by approximately 0.3−0.4 eV; the relative error increases slightly as the size of the ligand increases. LB94 generally predicts orbital energy differences that are approximately 0.1 eV higher than those from BP86; this model potential underestimates SAOP values by up to 0.08 eV for a triple-ζ basis set or up to 0.18 eV for a double-ζ basis set. In general, orbital energy differences predicted with a double-ζ basis set are 0.3−0.4 eV lower than those calculated with a triple-ζ basis set. Overall, the orbital energy differences with the greatest magnitudes (which correspond to excitation energies that are about 0.2 eV below experiment, as discussed above) are achieved by utilizing asymptotically correct model potentials with large basis sets.

For SCH_2CH_2Ph, the ligand used in experiments and the most sizable one considered here, calculations employing full core basis sets are not feasible on nodes with 32 GB RAM. Thus, SAOP calculations are not possible and orbital energy differences calculated using Xα, BP86, and LB94 may be compared for the four ligands. The trends for these three methods are similar, so only the LB94/DZ.4p results are discussed here. At the LB94/DZ.4p level of theory, the SH ligand overestimates energy difference *a* by 0.097 eV relative to *a* from the SCH_2CH_2Ph ligand, whereas SCH_3 and SCH_2CH_3 underestimate *a* by 0.003 and 0.007 respectively (Table 5). Energy difference b_1 is overestimated by 0.064 for SH and underestimated by 0.028 and 0.012 for SCH_3 and SCH_2CH_3, respectively. Energy difference b_2 is overestimated by 0.002 for SH and underestimated by 0.051 and 0.026 for SCH_3 and SCH_2CH_3. For these first three orbital energy differences, the SH ligand overestimates

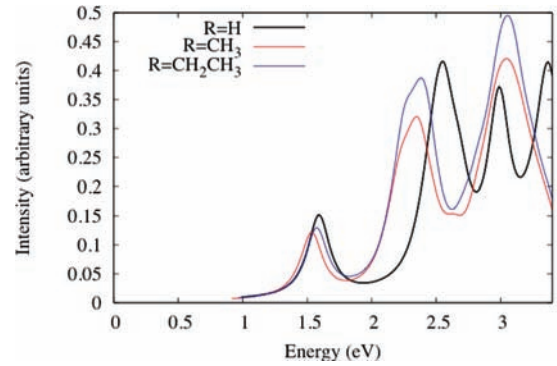

Figure 5. LB94/TZP.4f optical absorption spectrum for $Au_{25}(SR)_{18}^-$ (R = H, CH_3, CH_2CH_3) at their respective Xα/TZP.4f geometries.

the SCH_2CH_2Ph energy difference by approximately the same amount that SCH_3 and SCH_2CH_3 underestimate this quantity. At first glance, all three model ligands have difficulty with energy difference b_3, which is overestimated by 0.352, 0.313, and 0.373 for SH, SCH_3, and SCH_2CH_3, respectively. However for the nanoparticle with the SCH_2CH_2Ph ligand, the LUMO+3 orbital arises from the phenyl group. The next gold-based orbital lies 2.519 eV higher than the HOMO, which is in good agreement with b_3 values of 2.575, 2.538, and 2.592 eV predicted for SH, SCH_3, and SCH_2CH_3, respectively. Metal-to-ligand charge transfer will not be an issue for calculations of the excitation spectra of the three model ligands, but care is warranted in the use of TDDFT to compute the excitation spectrum of the full $Au_{25}(SCH_2CH_2Ph)_{18}^-$ nanoparticle due to potentially low-lying phenyl orbitals and the known[57] charge-transfer problems of TDDFT.

The overall variances between the calculated orbital energy differences for the four ligands are much smaller than the disparities observed for different methods and basis sets, as discussed further in the next section. The TDDFT excitation spectra at the LB94/TZP.4f level of theory for the SH, SCH_3, and SCH_2CH_3 model ligands are shown in Figure 5. The most significant difference in the spectra appears for peak *b*, which is predicted to lie approximately 0.15 eV lower in energy for SCH_3 and SCH_2CH_3 than for SH. Based on the orbital energy differences, peak *b* for the phenylethylthiol ligand is predicted to lie between 2.40−2.55 eV at this level of theory.

Basis Set/Model Potential Analysis. As discussed in the $Au_{25}(SH)_{18}^-$ optical absorption section above, the SAOP/TZP level of theory yields excitation energies that are within 0.2 eV of experiment. The dependence of the accuracy of the results as a function of basis set and model potential is of interest, particularly since the SAOP model requires full core basis sets that become impractical as the size of the system of interest increases. In Figure 6, absorption spectra calculated at the SAOP level of theory with DZ, TZP, and TZ2P basis sets at the Xα geometry are presented. Peak energies calculated with the DZ basis set lie 0.08−0.12 eV higher in energy than peak energies calculated with the TZP basis. Inclusion of a second polarization function (TZ2P) does not greatly affect the peak energies. TDDFT calculations on $Au_{25}(SH)_{18}^-$ with the QZ4P basis set are not possible on computers with 32 GB RAM.

Excitation spectra calculated with three asymptotically correct functionals and two GGAs are shown in Figure 7. For GRACLB calculations, the ionization potential is set to 0.11 au, the energy difference between anionic and neutral $Au_{25}(SH)_{18}$ at the Xα/TZP.4f level of theory. GRACLB calculations substantially underestimate the excitation energies relative to SAOP calculations. This has also been noted previously for Ag_{20}.[58] BP86 and

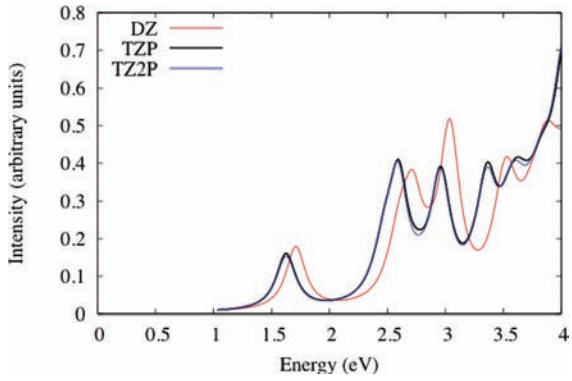

Figure 6. TDDFT optical absorption spectrum for $Au_{25}(SH)_{18}^-$ computed using SAOP with the listed basis sets at the Xα/TZP.4f geometry.

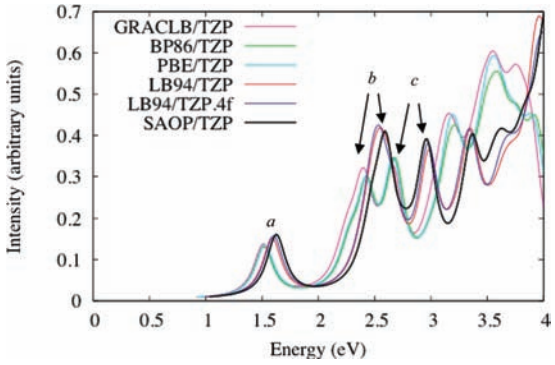

Figure 7. TDDFT optical absorption spectrum for $Au_{25}(SH)_{18}^-$ at the Xα/TZP.4f geometry using the levels of theory listed.

PBE calculations track the GRACLB results. Calculations employing LB94 with the full core TZP basis set vary slightly (<0.05 eV) from those utilizing SAOP. LB94 calculations involving the frozen core basis set TZP.4f differ from the full core value by 0.03 eV for peak *a* but exhibit essentially no change for peaks *b* and *c*. Thus, LB94 calculations with frozen core basis sets may provide a less expensive alternative with comparable accuracy to SAOP/TZP calculations.

Conclusions

The splitting between peaks *a* and *b* in the optical absorption spectrum arises as a result of ligand-field splitting of superatom D orbitals, and the value of this splitting is very sensitive to the gold−gold distances in the $Au_{25}(SH)_{18}^-$ nanoparticle core. In general, GGA's overestimate and LDA's very slightly underestimate Au−Au bond lengths in gold nanoparticles. Xα and Xonly with a triple-ζ basis set yield good agreement with structural parameters derived from X-ray crystal data, which suggests that these functionals may be useful in future structural predictions. However, the functionals used in geometry optimization should not necessarily be employed in TDDFT calculations of excitation energies because LDAs yield poor orbital energies for the $Au_{25}(SH)_{18}^-$ nanoparticle. Use of an asymptotically correct functional such as SAOP or LB94 yields excitation energies that lie 0.15−0.20 eV below the experimental peaks, where the difference may be due in part to self-interaction error. GRACLB, BP86, and PBE functionals further underestimate the excitation energies and yield absorption spectra with peak energies that differ substantially from experiment. If computational savings are required, frozen core LB94 calculations appear to provide an accurate alternative to full core SAOP computations.

Inclusion of implicit solvent in the calculations has negligible effects on the geometry and optical absorption spectrum of $Au_{25}(SH)_{18}^-$. However, modeling of the full experimental SCH_2CH_2Ph ligand by SH or SCH_3 introduces errors of several hundredths of an electronvolt in the first few peaks of the excitation spectrum, although this difference is slight compared to errors of several tenths of an electronvolt that can arise depending on the functional and basis set used in the calculation. Since the size of the ligand and the solvent play minor roles, this suggests that the geometric and electronic structure of the core is primarily responsible for the discrete optical absorption exhibited by this nanoparticle.

Acknowledgment. C.M.A. would like to thank Professor Robert Whetten for interesting discussions regarding the *a-b* peak splitting that inspired this work and Professor Rongchao Jin for sharing information regarding solvent effects on the experimental UV−vis spectrum. C.M.A. is grateful to Kansas State University for funding.

Supporting Information Available: This material is available free of charge via the Internet at http://pubs.acs.org.

References and Notes

(1) Jahn, W. *J. Struct. Biol.* **1999**, *127*, 106.
(2) Link, S.; Beeby, A.; FitzGerald, S.; El-Sayed, M. A.; Schaaff, T. G.; Whetten, R. L. *J. Phys. Chem. B* **2002**, *106*, 3410.
(3) Smith, R. K.; Nanayakkara, S. U.; Woehrle, G. H.; Pearl, T. P.; Blake, M. M.; Hutchison, J. E.; Weiss, P. S. *J. Am. Chem. Soc.* **2006**, *128*, 9266.
(4) Whetten, R. L.; Price, R. C. *Science* **2007**, *318*, 407.
(5) Wyrwas, R. B.; Alvarez, M. M.; Khoury, J. T.; Price, R. C.; Schaaff, T. G.; Whetten, R. L. *Eur. Phys. J. D* **2007**, *43*, 91.
(6) Zhu, M.; Qian, H.; Jin, R. *J. Am. Chem. Soc.* **2009**, *131*, 7220.
(7) Jadzinsky, P. D.; Calero, G.; Ackerson, C. J.; Bushnell, D. A.; Kornberg, R. D. *Science* **2007**, *318*, 430.
(8) Negishi, Y.; Nobusada, K.; Tsukuda, T. *J. Am. Chem. Soc.* **2005**, *127*, 5261.
(9) Balasubramanian, R.; Guo, R.; Mills, A. J.; Murray, R. W. *J. Am. Chem. Soc.* **2005**, *127*, 8126.
(10) Guo, R.; Song, Y.; Wang, G.; Murray, R. W. *J. Am. Chem. Soc.* **2005**, *127*, 2752.
(11) Heaven, M. W.; Dass, A.; White, P. S.; Holt, K. M.; Murray, R. W. *J. Am. Chem. Soc.* **2008**, *130*, 3754.
(12) Zhu, M.; Aikens, C. M.; Hollander, F. J.; Schatz, G. C.; Jin, R. *J. Am. Chem. Soc.* **2008**, *130*, 5883–5885.
(13) Akola, J.; Walter, M.; Whetten, R. L.; Häkkinen, H.; Grönbeck, H. *J. Am. Chem. Soc.* **2008**, *130*, 3756.
(14) Zhu, M.; Eckenhoff, W. T.; Pintauer, T.; Jin, R. *J. Phys. Chem. C* **2008**, *112*, 14221.
(15) Iwasa, T.; Nobusada, K. *J. Phys. Chem. C* **2007**, *111*, 45.
(16) Lopez-Acevedo, O.; Akola, J.; Whetten, R. L.; Grönbeck, H.; Häkkinen, H. *J. Phys. Chem. C* **2009**, *113*, 5035–5038.
(17) Cossaro, A.; Mazzarello, R.; Rousseau, R.; Casalis, L.; Verdini, A.; Kohlmeyer, A.; Floreano, L.; Scandolo, S.; Morgante, A.; Klein, M. L.; Scoles, G. *Science* **2008**, *321*, 943–946.
(18) Grönbeck, H.; Häkkinen, H.; Whetten, R. L. *J. Phys. Chem. C* **2008**, *112*, 15490–15492.
(19) Pei, Y.; Gao, Y.; Zeng, X. C. *J. Am. Chem. Soc.* **2008**, *130*, 7830.
(20) Chaki, N. K.; Negishi, Y.; Tsunoyama, H.; Shichibu, Y.; Tsukuda, T. *J. Am. Chem. Soc.* **2008**, *130*, 8608.
(21) Jiang, D.-e.; Tiago, M.; Luo, W.; Dai, S. *J. Am. Chem. Soc.* **2008**, *130*, 2777.
(22) Jiang, D.-e.; Luo, W.; Tiago, M. L.; Dai, S. *J. Phys. Chem. C* **2008**, *112*, 13905.
(23) Häkkinen, H.; Walter, M.; Grönbeck, H. *J. Phys. Chem. B* **2006**, *110*, 9927.
(24) Garzón, I. L.; Roviera, C.; Michaelian, K.; Beltrán, M. R.; Ordejón, P.; Junquera, J.; Sánchez-Portal, D.; Artacho, E.; Soler, J. M. *Phys. Rev. Lett.* **2000**, *85*, 5250.
(25) Garzón, I. L.; Reyes-Nava, J. A.; Rodríguez-Hernández, J. I.; Sigal, I.; Beltrán, M. R.; Michaelian, K. *Phys. Rev. B* **2002**, *66*, 073403.
(26) Häkkinen, H.; Barnett, R. N.; Landman, U. *Phys. Rev. Lett.* **1999**, *82*, 3264.
(27) de Heer, W. A. *Rev. Mod. Phys.* **1993**, *65*, 611.

(28) Walter, M.; Akola, J.; Lopez-Acevedo, O.; Jadzinsky, P. D.; Calero, G.; Ackerson, C. J.; Whetten, R. L.; Grönbeck, H.; Häkkinen, H. *Proc. Nat. Acad. Sci. U.S.A.* **2008**, *105*, 9157.
(29) Häkkinen, H. *Chem. Soc. Rev.* **2008**, *37*, 1847–1859.
(30) Aikens, C. M. *J. Phys. Chem. C* **2008**, *112*, 19797–19800.
(31) Vosko, S. H.; Wilk, L.; Nusair, M. *Can. J. Phys.* **1980**, *58*, 1200.
(32) Xu, X.; Goddard III, W. A. *Proc. Natl. Acad. Sci. U.S.A.* **2004**, *101*, 2673.
(33) Lee, C.; Yang, W.; Parr, R. G. *Phys. Rev. B* **1988**, *37*, 785.
(34) Handy, N. C.; Cohen, A. J. *Mol. Phys.* **2001**, *99*, 403.
(35) Perdew, J. P.; Burke, K.; Ernzerhof, M. *Phys. Rev. Lett.* **1996**, *77*, 3865.
(36) Keal, T. W.; Tozer, D. J. *J. Chem. Phys.* **2003**, *119*, 3015.
(37) Perdew, J. P.; Tao, J.; Staroverov, V. N.; Scuseria, G. E. *Phys. Rev. Lett.* **2003**, *91*, 146401.
(38) Adamo, C.; Barone, V. *J. Chem. Phys.* **1999**, *110*, 6158.
(39) Schmidt, M. W.; Baldridge, K. K.; Boatz, J. A.; Elbert, S. T.; Gordon, M. S.; Jensen, J. H.; Koseki, S.; Matsunaga, N.; Nguyen, K. A.; Su, S.; Windus, T. L.; Dupuis, M.; Montgomery, J. A, Jr. *J. Comput. Chem.* **1993**, *14*, 1347.
(40) Stevens, W. J.; Basch, H.; Krauss, M. *J. Chem. Phys.* **1984**, *81*, 6026.
(41) Stevens, W. J.; Krauss, M.; Basch, H.; Jasien, P. G. *Can. J. Chem.* **1992**, *70*, 612.
(42) Cundari, T. R.; Stevens, W. J. *J. Chem. Phys.* **1993**, *98*, 5555.
(43) Lovallo, C. C.; Klobukowski, M. *J. Comput. Chem.* **2003**, *24*, 1009.
(44) Lovallo, C. C.; Klobukowski, M. *J. Comput. Chem.* **2004**, *25*, 1206.
(45) te Velde, G.; Bickelhaupt, F. M.; Baerends, E. J.; Fonseca Guerra, C.; van Gisbergen, S. J. A.; Snijders, J. G.; Ziegler, T. *J. Comput. Chem.* **2001**, *22*, 931.
(46) van Lenthe, E.; Baerends, E. J.; Snijders, J. G. *J. Chem. Phys.* **1993**, *99*, 4597.
(47) van Leeuwen, R.; Baerends, E. J. *Phys. Rev. A* **1994**, *49*, 2421.
(48) Grüning, M.; Gritsenko, O. V.; van Gisbergen, S. J. A.; Baerends, E. J. *J. Chem. Phys.* **2001**, *114*, 652.
(49) Gritsenko, O. V.; Schipper, P. R. T.; Baerends, E. J. *Chem. Phys. Lett.* **1999**, *302*, 199.
(50) Schipper, P. R. T.; Gritsenko, O. V.; van Gisbergen, S. J. A.; Baerends, E. J. *J. Chem. Phys.* **2000**, *112*, 1344.
(51) Klamt, A.; Schüürmann, G. *J. Chem. Soc., Perkin Trans.* **1993**, *II*, 799.
(52) Pye, C. C.; Ziegler, T. *Theor. Chem. Acc.* **1999**, *101*, 396–408.
(53) Iwasa, T.; Nobusada, K. *Chem. Phys. Lett.* **2007**, *441*, 268.
(54) Rösch, N.; Nasluzov, V. A. *Chem. Phys.* **1996**, *210*, 415.
(55) Häberlen, O. D.; Chung, S.-C.; Stener, M.; Rösch, N. *J. Chem. Phys.* **1997**, *106*, 5189.
(56) Jin, R. private communication.
(57) Dreuw, A.; Head-Gordon, M. *J. Am. Chem. Soc.* **2004**, *126*, 4007.
(58) Aikens, C. M.; Li, S.; Schatz, G. C. *J. Phys. Chem. C* **2008**, *112*, 11272.

JP9051853